Multiscale characterization of the mineral phase at skeletal sites of breast cancer metastasis

Frank He[a], Aaron E. Chiou[a], Hyun Chae Loh[b], Maureen Lynch[a,c], Bo Ri Seo[a], Young Hye Song[a], Min Joon Lee[a], Rebecca Hoerth[d], Emely L. Bortel[d], Bettina M. Willie[e,f], Georg N. Duda[e], Lara A. Estroff[g,h], Admir Masic[b], Wolfgang Wagermaier[d], Peter Fratzl[d], and Claudia Fischbach[a,h,1]

[a]Nancy E. and Peter C. Meinig School of Biomedical Engineering, Cornell University, Ithaca, NY 14853; [b]Department of Civil and Environmental Engineering, Massachusetts Institute of Technology, Cambridge, MA 02139; [c]Department of Mechanical and Industrial Engineering, University of Massachusetts Amherst, Amherst, MA 01003; [d]Department of Biomaterials, Max Planck Institute of Colloids and Interfaces, 14424 Potsdam, Germany; [e]Julius Wolff Institut, Charité – Universitätsmedizin Berlin, 13353 Berlin, Germany; [f]Research Centre, Shriners Hospital for Children – Canada, Department of Pediatric Surgery, McGill University, Montreal, QC, Canada H4A 0A9; [g]Department of Materials Science and Engineering, Cornell University, Ithaca, NY 14853; and [h]Kavli Institute at Cornell for Nanoscale Science, Cornell University, Ithaca, NY 14853

Edited by Kristi S. Anseth, Howard Hughes Medical Institute, University of Colorado Boulder, Boulder, CO, and approved August 23, 2017 (received for review May 30, 2017)

Skeletal metastases, the leading cause of death in advanced breast cancer patients, depend on tumor cell interactions with the mineralized bone extracellular matrix. Bone mineral is largely composed of hydroxyapatite (HA) nanocrystals with physicochemical properties that vary significantly by anatomical location, age, and pathology. However, it remains unclear whether bone regions typically targeted by metastatic breast cancer feature distinct HA materials properties. Here we combined high-resolution X-ray scattering analysis with large-area Raman imaging, backscattered electron microscopy, histopathology, and microcomputed tomography to characterize HA in mouse models of advanced breast cancer in relevant skeletal locations. The proximal tibial metaphysis served as a common metastatic site in our studies; we identified that in disease-free bones this skeletal region contained smaller and less-oriented HA nanocrystals relative to ones that constitute the diaphysis. We further observed that osteolytic bone metastasis led to a decrease in HA nanocrystal size and perfection in remnant metaphyseal trabecular bone. Interestingly, in a model of localized breast cancer, metaphyseal HA nanocrystals were also smaller and less perfect than in corresponding bone in disease-free controls. Collectively, these results suggest that skeletal sites prone to tumor cell dissemination contain less-mature HA (i.e., smaller, less-perfect, and less-oriented crystals) and that primary tumors can further increase HA immaturity even before secondary tumor formation, mimicking alterations present during tibial metastasis. Engineered tumor models recapitulating these spatiotemporal dynamics will permit assessing the functional relevance of the detected changes to the progression and treatment of breast cancer bone metastasis.

breast cancer | bone metastasis | bone mineral nanostructure | X-ray scattering | Raman imaging

Eighty percent of advanced breast cancer patients develop metastases in bone (1). Following dissemination to the skeleton, metastatic breast cancer cells intimately interact with bone cells to facilitate seeding and expansion while disrupting homeostatic bone remodeling (1–3). The early-stage colonization of disseminated tumor cells appears to depend on active osteogenesis and adhesion to osteoblasts (4), whereas the eventual transition to macrometastasis involves a vicious cycle that promotes osteolytic activity through the aberrant activation of osteoclasts (1–3). While most studies have focused on identifying the cellular and molecular mechanisms underlying bone metastasis (1–4), very little is known about how breast cancer and bone metastasis alter the physical properties of the mineralized bone extracellular matrix (ECM).

The basic building block of the bone ECM is a nanocomposite of collagen fibrils and coaligned mineral crystals that underlie a unique hierarchical structure (5). Primarily composed of carbonated hydroxyapatite [$Ca_5(PO_4,CO_3)_3(OH)$] (HA), these mineral crystals are elongated platelets with thicknesses of ∼2–7 nm and with lengths on the order of 15–200 nm (5, 6). The physicochemical properties of HA (i.e., crystallinity, chemical composition, size, aspect ratio, and arrangement) dictate bone mechanical properties (5) and can vary as a function of disease, diet, age, and anatomical location (7–12). Notably, HA crystal size and orientation increase with bone tissue maturity (10–12). These variations, in turn, may modulate tumor progression. Studies with synthetically defined cell culture substrates have suggested that breast cancer cell adhesion, proliferation, and osteolytic factor expression are regulated by the materials properties of HA nanocrystals (13–15). However, the physiological relevance of these in vitro observations is unclear as it remains unresolved whether bone metastasis-relevant sites feature specific nanoscale HA materials properties and if these properties vary with cancer.

Previous in vivo studies of bone metastasis have used microcomputed tomography (μCT) or dual-energy X-ray absorptiometry to assess various bone indices such as bone mineral density, bone volume fraction, and trabecular number or thickness (16, 17). While these techniques have yielded important insights, they are not capable of resolving bone mineral properties at the nanometer length scale. We sought to address this gap in knowledge by using X-ray scattering, a nondestructive technique which can quantitatively assess the size (thickness via the T-parameter and length via the

Significance

Hydroxyapatite (HA) nanocrystals are key constituents of the bone extracellular matrix and thus likely to influence the pathogenesis of breast cancer skeletal metastasis. However, there is currently an insufficient understanding of HA nanocrystal properties at sites prone to bone metastasis formation. Here we report a novel application of X-ray scattering and Raman imaging to characterize HA nanostructure in mouse models of breast cancer. Our results suggest that bone regions linked with the initiation of metastasis contain less-mature HA nanocrystals and that mammary tumors enhance HA nanocrystal immaturity in these regions even prior to secondary tumor formation. Insights from this work will significantly advance the development of mineralized culture models to investigate how the bone microenvironment regulates breast cancer metastasis.

Author contributions: F.H., L.A.E., P.F., and C.F. designed research; F.H., A.E.C., H.C.L., M.L., B.R.S., Y.H.S., M.J.L., R.H., E.L.B., A.M., and W.W. performed research; G.N.D., A.M., and P.F. contributed new reagents/analytic tools; F.H., A.E.C., H.C.L., B.M.W., G.N.D., L.A.E., A.M., W.W., P.F., and C.F. analyzed data; and F.H. and C.F. wrote the paper.

The authors declare no conflict of interest.

This article is a PNAS Direct Submission.

[1]To whom correspondence should be addressed. Email: cf99@cornell.edu.

This article contains supporting information online at www.pnas.org/lookup/suppl/doi:10.1073/pnas.1708161114/-/DCSupplemental.

L-parameter) and arrangement (orientation via the ρ-parameter) of bone mineral nanocrystals (10, 18) (Fig. S1). To account for the spatial heterogeneity of bone mineral (5), X-ray scattering instruments can be programmed to scan larger micrometer-scale regions of interest. This technique has greatly contributed to the understanding of bone biomineralization, as it has been widely used to characterize HA nanocrystal structure across a range of organisms (e.g., humans, mice, rats, baboons, minipigs, and turkeys) (5) and has shown that even very small changes to these nanostructural features are linked to pathological conditions (19). Here, we have combined X-ray scattering with complementary imaging techniques that include large-area Raman imaging, backscattered electron microscopy (BSE), histology, and μCT. This multiscale approach allowed us to correlate HA nanostructural differences with bone tissue chemical composition and mineral crystallinity as well as cellularity and global changes in mineral distribution (Fig. 1). These studies provide the most-detailed-to-date assessment of bone hierarchical structure as it pertains to breast cancer and bone metastasis.

Results

In Tibiae of Healthy Mice, HA Nanocrystals Are More Immature in Regions Prone to Metastasis. In experimental mouse models of breast cancer bone metastasis, the tibia is a common site of secondary tumor formation (20, 21). Within the tibia, disseminated cancer cells appear to preferentially localize to the metaphysis rather than the diaphysis (20, 21), a phenomenon that has been attributed to specific cellular properties of metaphyseal blood vessels and an enrichment of chemoattractants (22). What is unclear, however, is whether the physical nature of bone mineral also varies between the metaphysis, which is largely comprised of trabecular bone, and the diaphysis, which is primarily dense cortical bone (23). To address this question, we applied laboratory-based small-angle X-ray scattering (SAXS) analysis (Fig. S1*A*) to establish a baseline of differences in HA nanocrystal thickness and orientation (Fig. 2*A*) between metaphyseal and diaphyseal bone in the tibiae of disease-free mice. We observed that mineral crystals in the metaphysis were

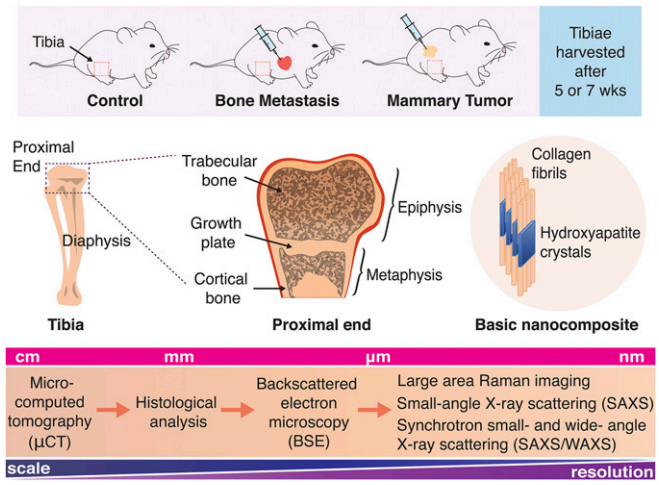

Fig. 1. Experimental setup for multiscale analysis of bone hierarchical structure. Different stages of human breast cancer were modeled in immunocompromised nude mice. To achieve bone metastasis, luciferase-labeled BoM1-2287 cells were intracardially injected, while injection into cleared mammary fat pads resulted in localized mammary tumors without overt metastasis. Mouse tibiae harvested after 5 or 7 wk were embedded in PMMA and subjected to μCT, histological analysis, and backscattered BSE to assess macro- to microscale changes in bone structure. SAXS and WAXS as well as large-area Raman imaging were used to characterize bone nanostructure and physicochemical composition.

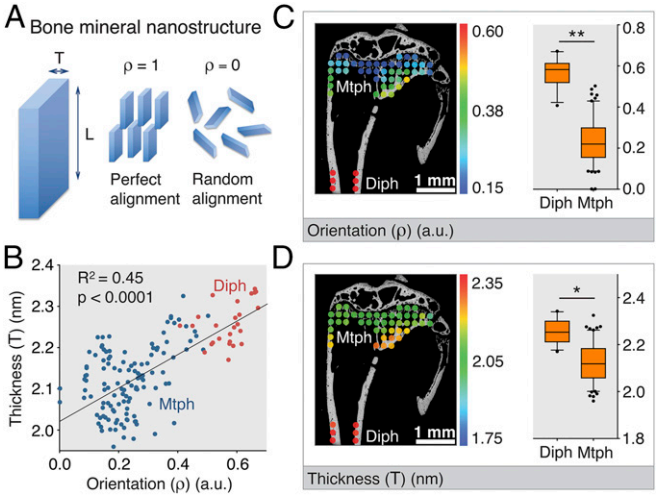

Fig. 2. Laboratory-based SAXS analysis of tibiae from healthy mice shows that HA nanocrystals in the metaphysis are more immature than ones in the diaphysis. (*A*) X-ray scattering techniques provide information on bone mineral nanostructure. (*B*) Correlation analysis between T-parameter and ρ-parameter as determined by simple linear regression. Data points represent individual measurements. The data are color-partitioned into two regions of interest (Diph, diaphysis; Mtph, metaphysis). (*C* and *D*) Spatial representation of quantitative data. Representative ρ-parameter (mean mineral crystal orientation) (*C*) and T-parameter (mean mineral crystal thickness) (*D*) data are overlaid on corresponding BSE images. Color scales: Warmer colors indicate greater crystal orientation (*C*) or thickness (*D*). Box-and-whisker plots of all ρ-parameter (*C*) and T-parameter (*D*) data from the regions of interest. Whiskers represent the 5th percentile and the 95th percentile. Outlier data points are depicted as dots. $*P < 0.05$, $**P < 0.001$.

significantly thinner (indicated by decreased T-parameter) and less oriented (indicated by decreased ρ-parameter) than those in the diaphysis (Fig. 2 *B–D*). In fact, crystals that were thinner were also less oriented (Fig. 2*B*), suggesting that the development of HA thickness and orientation occur in parallel. Our results are in strong agreement with previous studies that identified HA nanostructural heterogeneity in murine long bones (10, 24). The relative immaturity of metaphyseal HA crystals is consistent with their close proximity to the ossification center and the high turnover rate of metaphyseal trabecular bone (23). As breast cancer cells can adhere and proliferate better on smaller and less-perfect HA nanoparticles (13), the detected differences in metaphyseal versus diaphyseal HA nanostructure may be functionally relevant to the preferential metastatic tumor cell colonization of the proximal tibia.

Metastasis Initiation in the Proximal Tibial Metaphysis Alters the Bone ECM. We next performed a multiscale characterization of tibial metastasis to identify tumor-mediated changes of bone ECM in these sites. To achieve bone metastasis, we injected luciferase-expressing BoM1-2287 breast cancer cells, a bone metastatic subpopulation of the MDA-MB-231 cell line (21), into the left ventricle of the mouse heart. As expected, this approach resulted in the reliable formation of macrometastasis in the proximal tibiae of immunocompromised BALB/c nude mice after 5 wk (21) (Fig. S2*A*). μCT scans (Fig. 3 *A* and *C*), Movat's pentachrome staining (Fig. 3 *B* and D and Fig. S3), and BSE images (Fig. S4) revealed massive degradation of metaphyseal trabecular bone. Viewed at these length scales, macrometastatic outgrowths were largely contained in the metaphysis, did not occur in the epiphysis (Fig. S3), and left diaphyseal cortical bone unaffected (Fig. S4). Growth plate integrity was severely compromised in bone metastasis versus control samples, as suggested by the presence of fibrous tissue (25) rather than the organized arrays of chondrocyte

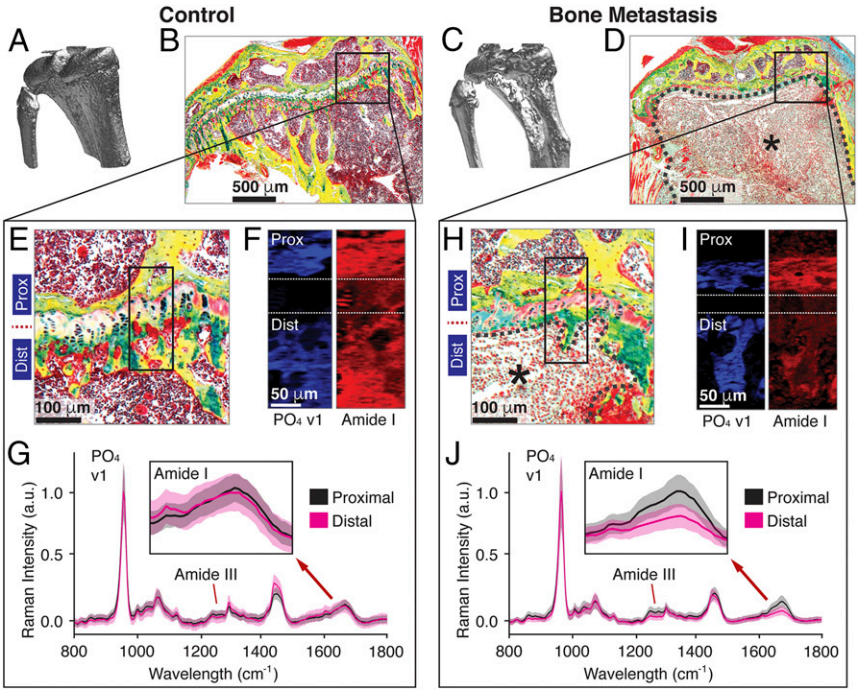

Fig. 3. Multiscale characterization of the bone metastatic site identifies changes in the ECM associated with secondary tumor formation. (*A–D*) Macro- to microscale qualitative analysis: Representative μCT images (*A* and *C*) and Movat's pentachrome (MP)-stained cross-sections (*B* and *D*). Color legend of the MP stain: yellow, bone; green, calcified cartilage; black, nuclei; intense red, muscle; red/pink, fibrous tissue. The metastasized tumor is highlighted by the black asterisk and outlined with dashed lines (*D*). (*E–J*) Nanoscale quantitative analysis: large-area Raman imaging of defined regions (black insets) (*E* and *H*). "Prox" and "Dist" (*E*, *F*, *H*, and *I*) indicate bone on the proximal (i.e., the epiphysis) and distal (i.e., the metaphysis) sides of the growth plate, respectively. The metastasized tumor is highlighted by the black asterisk and outlined with dashed lines (*H*). False color heat maps (*F* and *I*): Blue and red depict the intensities of the PO_4 v1 and amide I peaks, respectively. Mean Raman spectra (bold line: means; fill areas: SD) (*G* and *J*) of the indicated bone regions with insets (range: 1,600–1,700 cm^{-1}) highlighting the amide 1 peak (1,677 cm^{-1}).

columns (Fig. S3). These observations support the possibility that disseminated tumor cells preferentially entered the tibiae through sinusoidal vessels supplying the metaphyseal trabecular bone (22) and that the growth plate acted as a barrier preventing tumor cell advancement to the epiphysis.

We were specifically interested in characterizing the compositional and structural properties of tumor-interfacing bone remnants of what was once a mesh of metaphyseal trabecular bone (Figs. S3 and S4). To this end, we used large-area Raman imaging to compare the chemical signatures of trabecular bone proximal (i.e., the epiphysis) and distal (i.e., the metaphysis) to the growth plate in control and metastasis conditions (Fig. 3 *E–J*). Interestingly, in both control and tumor-bearing tibiae we observed that the intensity of the PO_4 v1 peak (960 cm^{-1}) was comparable between the metaphysis and the epiphysis (Fig. 3 *F* and *I*). This result suggests that the immediate presence of a tumor has little effect on the mineral content of the remaining bone (26). In contrast, we found pronounced spectral differences in the amide I peak (1,677 cm^{-1}), a proxy for collagen type I content (26), between the metaphysis and epiphysis of metastasis-associated bones (Fig. 3 *I* and *J*). Because the intensity of the amide I peak is polarization-dependent and may be affected by polarization orientation of the incident beam, we also assessed the intensity of the polarization-independent amide III peak (1,256 cm^{-1}) (26, 27), which exhibited a concomitant decrease (Fig. S5*B*). In contrast, the amide I and III peaks were virtually unaffected in the tibial metaphysis of control mice (Fig. 3 *F* and *G* and Fig. S5*A*). Hence, a significant increase in the phosphate-to-amide (PO_4/Amide I) ratio ($P < 0.05$) was observed in the bone metastasis condition versus the control condition (Fig. S6). Collectively, these data suggest a decrease in collagen relative to mineral content within bone that is in physical contact with the secondary tumor.

While the mineral content in the remnant bone tissue may have not been affected by the immediate presence of a tumor (Fig. 3*I* and Figs. S4 and S6*B*), bone mineral nanostructure may still have been impacted (8, 9, 28). As such, we were also interested in assessing changes in HA nanostructure within metastasis-associated bone remnants. Targeting these bone remnants with X-ray scattering techniques proved technically infeasible, however. As an alternative, we derived mineral crystallinity—a measure of HA nanocrystal maturity—from the inverse of the Raman PO_4 v1 peak FWHM (8, 29). This parameter positively correlates with the stoichiometric perfection and length of the crystallites along the *c* axis (29). Interestingly, we found that mineral crystallinity in the bone remnants was markedly decreased ($P < 0.05$) in the bone metastasis condition relative to the control (Fig. S7). Taken together, the immediate presence of a tumor may promote the decrease of mineral maturity along with reduced collagen content.

Metaphyseal HA Nanostructure is Altered by the Presence of a Localized Mammary Tumor. Next, we asked if the bone ECM can be altered by the presence of a localized primary tumor. While previous studies of bone metastasis have shown that circulating biomolecules can modulate bone cell activity (30) and bone collagen remodeling (31), our focus here was to investigate the possibility of premetastatic changes in the mineral nanostructure of bone. To recapitulate a scenario of breast cancer without evident bone metastases, we implanted the same BoM1-2287 cells into the mammary fat pads of BALB/c nude mice, which, over a period of 7 wk, enabled primary tumor growth but did not result in metastatic outgrowth (32) (Fig. S2*B*) or the physical wasting associated with cachexia (Fig. S2*C*). Complementary techniques with resolutions spanning the macro- to microlength scales did not reveal primary tumor-mediated changes in metaphyseal bone. Histological staining, BSE imaging, and μCT analysis suggested that the cellular composition (Fig. S8*A*), mineral density (Fig. S8*A*), and trabecular bone structure (Fig. S8*B*) was similar between the tibial metaphysis of control mice and mice carrying primary mammary tumors.

We then used X-ray scattering analysis to examine potential primary tumor-mediated changes in bone nanostructure. Laboratory-based SAXS did not indicate differences in HA nanocrystal orientation and thickness in metaphyseal bone between control and mammary tumor groups (Table S1). However, since tumor-mediated differences in the mineral phase could conceivably occur on extremely small length scales, we hypothesized that the spatial resolution of laboratory-based SAXS (Fig. S1*A*) may have been insufficient to detect these possible changes in

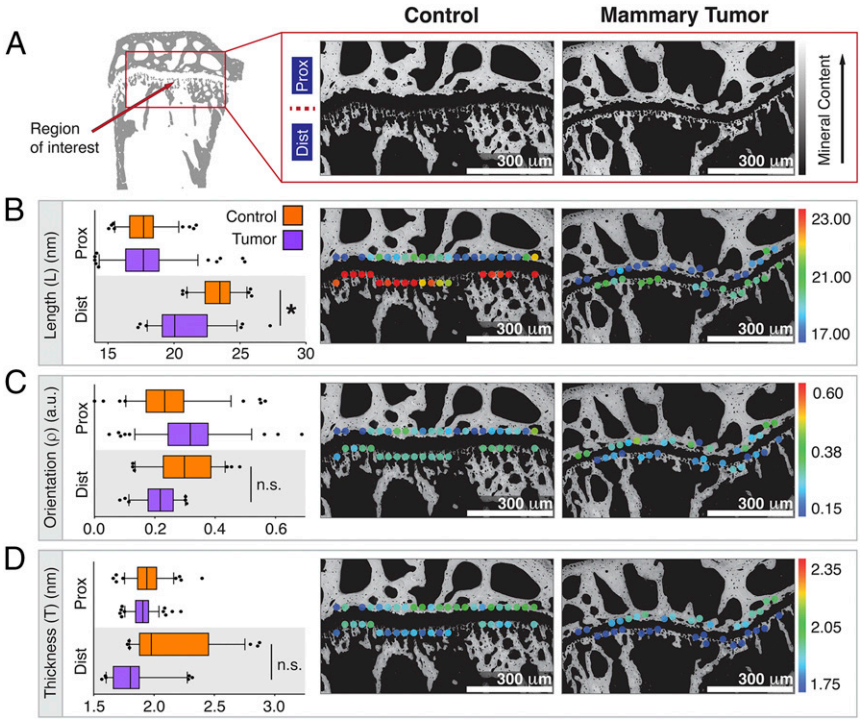

Fig. 4. Scanning synchrotron-based SAXS/WAXS analysis of metaphyseal tissue bordering the growth plate reveals shorter HA nanocrystals in mice carrying mammary tumors. (*A*) Representative BSE images of the region of interest. Prox and Dist indicate the proximal and distal sides of the growth plate, respectively. (*B–D*) Spatial representation of quantitative data. Box-and-whisker plots summarize all L-parameter (mean mineral crystal length) (*B*), ρ-parameter (mean mineral crystal orientation) (*C*), and T-parameter (mean mineral crystal thickness) (*D*) data. Whiskers represent the 5th and the 95th percentile. Outlier data points are depicted as dots. $*P < 0.05$. n.s. indicates nonsignificance. Representative L-parameter (*B*), ρ-parameter (*C*), and T-parameter (*D*) data are overlaid on corresponding BSE images. Color scales: Warmer colors indicate greater crystal length (*B*), orientation (*C*), or thickness (*D*).

HA. Therefore, we next analyzed the samples using scanning synchrotron-based SAXS and wide-angle X-ray scattering (WAXS) (Fig. S1*B*). In addition to providing information on mineral crystal thickness and orientation from SAXS, this approach also enables the derivation of the mineral crystal length (L-parameter) from WAXS (Fig. S1*B*). Given that the growth plate is a region of high metabolic activity and mineralization (23), we focused our analysis on the HA mineral within 50 μm of the growth plate cartilage. Here, we observed tumor-mediated changes in mineral crystal nanostructure, which were dependent on the location of the scanned mineral (Fig. 4). More specifically, HA mineral crystals immediately distal to the growth plate were significantly shorter in tibiae from mice with mammary tumors versus control mice (Fig. 4*B*). A downward, though nonsignificant, trend was also detected in both mineral crystal orientation ($P = 0.33$) (Fig. 4*C*) and thickness ($P = 0.56$) (Fig. 4*D*). This observed decrease in HA nanocrystal size was corroborated with Raman imaging measurements of corresponding bone regions, which suggested that mineral crystallinity was decreased ($P < 0.05$) in the mammary tumor condition relative to that of the control (Fig. S7). Furthermore, these differences mimicked measurements of mineral crystallinity in the bone remnants physically adjoined to a metastatic tumor mass (Fig. S7). During murine bone development HA crystals undergo large increases in length while thickness stays relatively constant (10), which could suggest that HA length is more susceptible to aberrant perturbations. Interestingly, these tumor-mediated changes were only observed in the tissue distal but not proximal to the growth plate (Fig. 4 *B–D*), which is consistent with the preferential initiation of secondary tumors in the metaphysis rather than in the epiphysis (Fig. 3 and Fig. S3).

To explore possible mechanisms by which a mammary tumor could remotely alter metaphyseal bone mineral, we assessed markers of bone matrix remodeling in tibiae harvested from mice systematically conditioned with daily i.p. injections of tumor-derived media over the course of 3 wk. Picrosirius Red-stained cross-sections of the proximal tibiae revealed a significant increase in the collagen content of metaphyseal trabecular bone (Fig. S9*A*) while tartrate-resistant acid phosphatase (TRAP) staining of this same region revealed no difference in the number of osteoclasts (Fig. S9*B*). These data suggest that in a skeletal region prone to metastasis, circulating tumor-derived factors can lead to an increase in local osteogenesis, while leaving bone resorption unaffected. Accordingly, culturing bone marrow-derived mesenchymal stem cells (MSCs) in the same tumor-derived media resulted in elevated matrix calcification via Alizarin Red S (ARS) staining compared with controls (Fig. S9*C*), which is indicative of tumor factor-mediated osteogenic differentiation. Importantly, this trend was more pronounced ($P < 0.05$) when MSCs were cultured in media from the bone metastatic cells used in our bone mineral characterization studies (BoM1-2287) relative to the parental cell line (Fig. S9*C*). Taken together, these results imply that factors secreted from bone metastatic breast cancer cells can aberrantly promote local osteogenesis by altering the fate of bone marrow-residing MSCs. Increased osteogenesis may explain the enhanced HA immaturity at metastatic sites, as newly formed bone is typically composed of smaller, less-perfect, and less-oriented HA crystals (6).

Discussion

Interactions between breast cancer cells and the bone microenvironment are critical to the pathogenesis of skeletal metastases, but the associated nanostructural changes of bone mineral remain unclear. Gaining an improved understanding of this potential relationship is critical as HA nanocrystal properties can significantly alter cellular phenotypes (13–15) and, thus, conceivably affect malignancy. Using a combination of high-resolution analytical techniques to characterize tibiae from mouse models of bone metastatic and localized breast cancer, we show that the nanostructure of HA crystals varies between anatomical regions that are more and less prone to metastatic colonization, and that primary tumors may reinforce these variations even before metastatic outgrowth.

The observation that breast cancer cells preferentially colonize the proximal tibial metaphysis may have broader pathological relevance. Adjacent to a secondary ossification center

and enriched with trabecular bone (23), the tibial metaphysis of young mice can exemplify a distinct anatomical site of high bone turnover (i.e., resorption of old bone followed by formation of new bone). Clinicians have long observed preferential metastatic localization to sites of active remodeling (33), such as the trabecular bone-rich pelvis and spinal vertebral bodies (2, 33). As the nanostructure of human and murine bone mineral is similar (5, 10), it is likely that HA crystals in these metabolically more active human skeletal sites are also more immature. Future studies will need to confirm this possibility and assess the functional role of HA materials properties in driving secondary tumor formation in these sites.

Furthermore, our SAXS/WAXS and Raman data point to a potential mammary tumor-mediated increase of local osteogenesis in the initial trabecular network before secondary tumor formation. This finding supports experimental evidence by others that primary tumors can activate premetastatic remodeling of the bone, and that these changes ultimately promote metastatic dissemination (30, 31). While these previous studies of mammary tumor-mediated changes focused on bone cell activity (30) and circulating markers of bone collagen remodeling (31), our data now additionally suggest that structural changes occur in the mineral phase of bone. More specifically, we observed a decrease in mineral nanocrystal size in the metaphyseal bone tissue bordering the growth plate. Since these changes occurred at a bone growth front, these data indicate that a localized mammary tumor may be affecting the mineralization of new matrix. In bone, the deposition of HA results from a thermodynamically driven cascade that may involve the initial formation of disordered, less stable nanoparticulate phases that become more crystalline and increase in size as they progress to the final mineral phase (34, 35). As such, a mammary tumor could conceivably decrease general mineral maturity by releasing factors that stimulate osteogenic cells to increase their production of new bone (Fig. S9), which typically consists of smaller, less-perfect and less-oriented HA crystals (6). Alternatively, the physiological maturation of bone mineral could also be directly inhibited by soluble factors secreted by the mammary tumor. The glycoprotein osteopontin is a potential candidate, as it is highly expressed by the BoM1-2287 cells (21) used in this study and is known to inhibit the growth of HA mineral (36). Furthermore, changes in HA nanostructure may have been due to mammary tumor-mediated effects on the longitudinal bone growth of the young mice (37) used in our studies. However, given the similarities in growth plate thicknesses (Fig. S2*D*) and trabecular network properties (Fig. S8 *A* and *B*) between control tibiae and mammary tumor-associated tibiae, the metabolic program of growth plate chondrocytes and the consequent rate of endochondral ossification (38) appear to be unaffected by the primary tumors. Taken together, our results suggest that the primary mammary tumor could induce the formation of less-mature bone mineral in the absence of a secondary tumor, likely without changing overall skeletal growth.

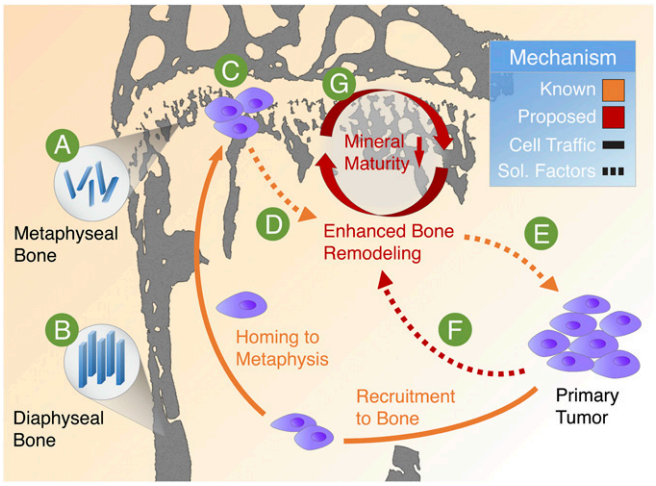

Fig. 5. Proposed functional relationship between HA mineral characteristics and breast cancer bone metastasis. In mice, breast cancer cells typically colonize the metaphysis in the metabolically active proximal tibia. We show that mineral in metaphyseal bone (*A*) is less mature (i.e., smaller, less-perfect, and less-oriented) relative to other skeletal locations (*B*) not prone to initiation of metastasis. Because previous in vitro findings show that tumor cells preferentially adhere to less-mature crystals, we propose that this difference in mineral properties may be functionally relevant to the establishment of a tumor colony (*C*). The metastasized tumor cells can then disrupt typical bone remodeling processes (*D*) to result in the aberrant activity of bone cells and the increased release of tumor-recruiting soluble factors (*E*). Furthermore, breast cancer cells located within primary tumors can stimulate bone remodeling by secreting circulating factors (*F*) that enhance local osteogenesis and, thus, alter the composition and structure of the bone ECM. Here, we propose that these premetastatic changes lead to the deposition of a less-mature mineral phase (*G*) which may be essential in driving the vicious cycle of osteolytic bone metastasis.

Premetastatic, primary tumor-mediated changes in nanoscale bone mineral properties may be an underappreciated mechanism that could play a role in the initial establishment and survival of a secondary tumor colony in the bone. Because metastatic breast cancer cells exhibit increased proliferation and adhesion on smaller and less-perfect HA nanocrystals (13), these early-stage changes of bone mineral may promote the initial seeding and survival of disseminated tumor cells. Furthermore, the deposition of a more immature mineral phase that is more susceptible to osteolytic degradation (39, 40) could facilitate the vicious cycle of bone metastasis, thus promoting tumor outgrowth. Complemented by our previous work suggesting that nanoscale HA materials properties can influence breast cancer malignant progression (13–15), we propose a modified view of the vicious cycle of bone metastasis in which HA materials properties are functionally linked with the pathogenesis of breast cancer bone metastasis (Fig. 5). Detailed in vivo studies will be needed to conclusively define the functional consequences of our observations. Nevertheless, our results bring to light that nanostructural parameters of the bone metastatic site are currently underappreciated but should be considered when studying the microenvironmental complexities that influence bone metastasis.

While others have previously reported that breast cancer can remotely engender bone destruction (16, 30, 31), we now further advance this field of work by quantifying tumor-mediated changes in HA nanostructure in skeletal locations associated with metastasis. The findings here may inform future therapeutic strategies. For instance, adjuvant prescription of antiresorptive drugs such as bisphosphonates (BPs) is currently largely palliative and does not improve patient survival rate (1). BPs, which are taken up by bone-resorbing osteoclasts, localize to mineralized tissue by selectively binding to HA (1). As molecular simulation studies show that BP–HA binding energies are dependent on HA nanocrystal size (41), BP therapeutic efficacy may be affected by tumor-induced changes in HA nanostructure. Understanding how nanoscale variations in HA structure affect BP binding may aid the development of derivatives and protein conjugates (42) that are more effective in the treatment of bone metastasis.

Although limited by sample throughput, X-ray scattering analysis and large-area Raman imaging generate position-resolved information on the micro- to nanoscales that can be combined with a host of other techniques to provide a comprehensive assessment of bone materials properties in a variety of pathological contexts. Thus, similar approaches to the one described in this paper can be used to assess bone nanostructure in animal models of other cancers (e.g., prostate and

lung) that also metastasize to bone (2). Insights from these analyses will inform the design of biomimetic culture systems (43) and high-throughput screening platforms (44) to investigate the functional role of HA mineral in bone metastasis as well as the development of tissue-engineered tumor models that recapitulate the bone microenvironment (45). Moreover, future work will also need to consider the effect of changing bone mineral properties in the context of the intimately associated collagen fibrils and adhesive proteins enriched in the metastatic site. Interdisciplinary collaborations between the fields of biomaterials, cancer biology, and oncology will be key to this promising new field of work in which materials science approaches will play an important role.

Materials and Methods

Detailed descriptions are provided in *SI Materials and Methods*.

Mouse Models of Breast Cancer. Three-week-old, female BALB/c nude mice (Taconic) were used for animal studies. Intracardiac injections of luciferase-labeled BoM1-2287 cells led to tibial metastases while mammary fat pad injections generated localized mammary tumors. Tibiae were harvested at 5 (bone mets) or 7 wk (mam tumor), fixed in 70% EtOH (48 h), and embedded in polymethylmethracrylate (PMMA). All animal studies were performed in accordance with protocols approved by Cornell University's Institutional Animal Care and Use Committee.

Macro- to Microscale Analysis. Samples were scanned via μCT (BrukerCT; Scanco) and trabecular bone outcomes (BV/TV, Tb.Th, and Tb.Sp) were compared ($n = 3$). Backscattered SEM (FEI) and Movat's pentachrome staining were performed on longitudinal cross-sections.

X-Ray Scattering. Lab SAXS (Bruker) was performed across the proximal tibiae and on select diaphyseal bone of longitudinal sections while synchrotron SAXS/WAXS (BESSY II) was performed on bone bordering the growth plate and on select diaphyseal bone. The sample size was at least $n = 3$. The T-, ρ-, and L-parameters were calculated as previously described (10, 18). A mixed model was used for statistical analyses.

Large-Area Raman Imaging. Raman imaging (WiTec) was performed on select regions of representative longitudinal sections. PO_4 v1 (960 cm^{-1}), amide I (1,677 cm^{-1}), and amide III (1,256 cm^{-1}) peaks were fitted with Gaussian functions and their intensities as well as FWHMs were extracted. After excluding outlier data, the means and SDs were calculated. A two-sample *t* test was used to assess differences between regions.

ACKNOWLEDGMENTS. We thank C. Li, S. Siegel, and I. Zenke for assistance with SAXS/WAXS; and F. Vermeylen for consultation with statistical analysis. BoM1-2287 cells were a gift from J. Massagué. This work was funded by NIH Grant R01CA173083, National Cancer Institute Grants 1U54CA199081-01 and 1U54CA210184-01, an NSF fellowship (to F.H.), and an A. v. Humboldt fellowship (to C.F.).

1. Kozlow W, Guise TA (2005) Breast cancer metastasis to bone: Mechanisms of osteolysis and implications for therapy. *J Mammary Gland Biol Neoplasia* 10:169–180.
2. Ren G, Esposito M, Kang Y (2015) Bone metastasis and the metastatic niche. *J Mol Med (Berl)* 93:1203–1212.
3. Weilbaecher KN, Guise TA, McCauley LK (2011) Cancer to bone: A fatal attraction. *Nat Rev Cancer* 11:411–425.
4. Wang H, et al. (2015) The osteogenic niche promotes early-stage bone colonization of disseminated breast cancer cells. *Cancer Cell* 27:193–210.
5. Fratzl P, Gupta HS, Paschalis EP, Roschger P (2004) Structure and mechanical quality of the collagen-mineral nano-composite in bone. *J Mater Chem* 14:2115–2123.
6. Olszta MJ, et al. (2007) Bone structure and formation: A new perspective. *Mater Sci Eng Rep* 58:77–116.
7. Boskey A, Mendelsohn R (2005) Infrared analysis of bone in health and disease. *J Biomed Opt* 10:031102.
8. Bi X, et al. (2013) Prostate cancer metastases alter bone mineral and matrix composition independent of effects on bone architecture in mice—a quantitative study using microCT and Raman spectroscopy. *Bone* 56:454–460.
9. Burke M, et al. (2017) The impact of metastasis on the mineral phase of vertebral bone tissue. *J Mech Behav Biomed Mater* 69:75–84.
10. Lange C, et al. (2011) Fetal and postnatal mouse bone tissue contains more calcium than is present in hydroxyapatite. *J Struct Biol* 176:159–167.
11. Bigi A, et al. (1997) Chemical and structural characterization of the mineral phase from cortical and trabecular bone. *J Inorg Biochem* 68:45–51.
12. Kuhn LT, et al. (2008) A comparison of the physical and chemical differences between cancellous and cortical bovine bone mineral at two ages. *Calcif Tissue Int* 83:146–154.
13. Pathi SP, Lin DDW, Dorvee JR, Estroff LA, Fischbach C (2011) Hydroxyapatite nanoparticle-containing scaffolds for the study of breast cancer bone metastasis. *Biomaterials* 32:5112–5122.
14. Choi S, Coonrod S, Estroff L, Fischbach C (2015) Chemical and physical properties of carbonated hydroxyapatite affect breast cancer cell behavior. *Acta Biomater* 24:333–342.
15. Wu F, et al. (2017) Protein-crystal interface mediates cell adhesion and proangiogenic secretion. *Biomaterials* 116:174–185.
16. Thorpe MP, et al. (2011) Breast tumors induced by N-methyl-N-nitrosourea are damaging to bone strength, structure, and mineralization in the absence of metastasis in rats. *J Bone Miner Res* 26:769–776.
17. Lynch ME, et al. (2013) In vivo tibial compression decreases osteolysis and tumor formation in a human metastatic breast cancer model. *J Bone Miner Res* 28:2357–2367.
18. Pabisch S, Wagermaier W, Zander T, Li C, Fratzl P (2013) Imaging the nanostructure of bone and dentin through small- and wide-angle X-ray scattering. *Methods in Enzymology*, ed De Yoreo JJ (Academic, New York), pp 391–413.
19. Fratzl P, Gupta HA, Roschger P, Klaushofer K (2009) Bone nanostructure and its relevance for mechanical performance, disease, and treatment. *Nanotechology* (Wiley-VCH, Weinheim, Germany), Vol 5, pp 345–360.
20. Wright LE, et al. (2016) Murine models of breast cancer bone metastasis. *Bonekey Rep* 5:804.
21. Kang Y, et al. (2003) A multigenic program mediating breast cancer metastasis to bone. *Cancer Cell* 3:537–549.
22. Mastro AM, Gay CV, Welch DR (2003) The skeleton as a unique environment for breast cancer cells. *Clin Exp Metastasis* 20:275–284.
23. Clarke B (2008) Normal bone anatomy and physiology. *Clin J Am Soc Nephrol* 3:S131–S139.
24. Tesch W, et al. (2003) Orientation of mineral crystallites and mineral density during skeletal development in mice deficient in tissue nonspecific alkaline phosphatase. *J Bone Miner Res* 18:117–125.
25. Joiner DM, et al. (2014) Accelerated and increased joint damage in young mice with global inactivation of mitogen-inducible gene 6 after ligament and meniscus injury. *Arthritis Res Ther* 16:R81.
26. Gamsjaeger S, Kazanci M, Pachalis EP, Fratzl P (2009) Raman application in bone imaging. *Raman Spectroscopy for Soft Matter Applications*, ed Maher SA (Wiley, New York), pp 227–267.
27. Kazanci M, Roschger P, Paschalis EP, Klaushofer K, Fratzl P (2006) Bone osteonal tissues by Raman spectral mapping: Orientation-composition. *J Struct Biol* 156:489–496.
28. Bloebaum RD, Skedros JG, Vajda EG, Bachus KN, Constantz BR (1997) Determining mineral content variations in bone using backscattered electron imaging. *Bone* 20:485–490.
29. Yerramshetty JS, Akkus O (2008) The associations between mineral crystallinity and the mechanical properties of human cortical bone. *Bone* 42:476–482.
30. Cox TR, et al. (2015) The hypoxic cancer secretome induces pre-metastatic bone lesions through lysyl oxidase. *Nature* 522:106–110.
31. Kelly T, et al. (2005) Expression of heparanase by primary breast tumors promotes bone resorption in the absence of detectable bone metastases. *Cancer Res* 65:5778–5784.
32. Kuperwasser C, et al. (2005) A mouse model of human breast cancer metastasis to human bone. *Cancer Res* 65:6130–6138.
33. Togawa D, Lewandrowski DU (2006) The pathophysiology of spinal metastases. *Cancer in the Spine*, ed McLain RF (Humana, New York), pp 17–24.
34. De Yoreo JJ, et al. (2015) Crystallization by particle attachment in synthetic, biogenic, and geologic environments. *Science* 349:aaa6760–aaa6760.
35. Mahamid J, et al. (2011) Bone mineralization proceeds through intracellular calcium phosphate loaded vesicles: A cryo-electron microscopy study. *J Struct Biol* 174:527–535.
36. George A, Veis A (2008) Phosphorylated proteins and control over apatite nucleation, crystal growth, and inhibition. *Chem Rev* 108:4670–4693.
37. Jilka RL (2013) The relevance of mouse models for investigating age-related bone loss in humans. *J Gerontol A Biol Sci Med Sci* 68:1209–1217.
38. Piao J, et al. (2013) Sirt6 regulates postnatal growth plate differentiation and proliferation via Ihh signaling. *Sci Rep* 3:3022.
39. Nagano M, Nakamura T, Kokubo T, Tanahashi M, Ogawas M (1996) Differences of bone bonding ability and degradation behaviour in vivo between amorphous calcium phosphate and highly crystalline hydroxyapatite coating. *Biomaterials* 17:1771–1777.
40. Barry AB, Baig AA, Miller SC, Higuchi WI (2002) Effect of age on rat bone solubility and crystallinity. *Calcif Tissue Int* 71:167–171.
41. Wright JE, Zhao L, Choi P, Uludag H (2004) Simulating hydroxyapatite binding of bone-seeking bisphosphonates. *Adv Exp Med Biol* 553:139–148.
42. Gittens SA, Bansal G, Zernicke RF, Uludağ H (2005) Designing proteins for bone targeting. *Adv Drug Deliv Rev* 57:1011–1036.
43. Murphy WL, Hsiong S, Richardson TP, Simmons CA, Mooney DJ (2005) Effects of a bone-like mineral film on phenotype of adult human mesenchymal stem cells in vitro. *Biomaterials* 26:303–310.
44. Barney LE, et al. (2015) A cell-ECM screening method to predict breast cancer metastasis. *Integr Biol* 7:198–212.
45. Seib FP, Berry JE, Shiozawa Y, Taichman RS, Kaplan DL (2015) Tissue engineering a surrogate niche for metastatic cancer cells. *Biomaterials* 51:313–319.